THE JOURNAL OF PHYSICAL CHEMISTRY C
A JOURNAL OF THE AMERICAN CHEMICAL SOCIETY

Unexpectedly High Electronic Partial Conductivity of Porous Yttria-Stabilized Zirconia Thin Films

Erdogan Celik, Adrian Usler, Miguel Wiche, Andrey Mazilkin, Torsten Brezesinski, Roger A. De Souza, and Matthias T. Elm*

Cite This: *J. Phys. Chem. C* 2025, 129, 12585−12594 Read Online

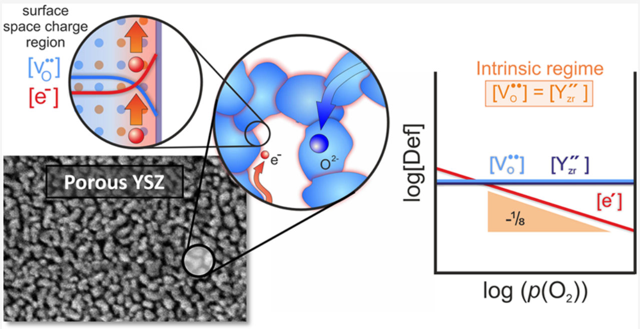

ABSTRACT: In porous form, ion conductors are key components for a vast number of applications, making detailed understanding of the impact of high surface area on electrochemical properties indispensable. Here, we report on the electrical characterization of dense and porous yttria-stabilized zirconia (YSZ) thin films deposited by pulsed laser deposition. While dense films exhibit high and dominant ionic conductivity over a wide oxygen partial pressure range, as expected for YSZ, porous films reveal an unexpectedly high electronic partial conductivity, which determines the transport properties under highly reducing conditions. By means of continuum simulations, we demonstrate that the high electronic conductivity contribution may be explained in terms of a space-charge region at the free surface, where electrons accumulate due to the positive surface charge. The latter results in increased electronic conductivity in the space-charge region, which dominates the transport properties of the porous thin films under highly reducing conditions. The results emphasize the importance of considering surface effects in nanostructured ion conductors for tailoring the overall electrochemical properties for device applications.

Oxygen-ion conducting ceramics play an important role in modern energy technologies. In particular, yttria-stabilized zirconia (YSZ) is extensively used as solid electrolyte, e.g., for solid oxide fuel cells (SOFCs),[1−3] oxygen permeation membranes,[4−6] or oxygen sensors,[7,8] due to its high oxygen-ion conductivity at elevated temperatures. The ionic conductivity dominates the overall electrical properties of single crystals of YSZ, with the electronic partial conductivity being more than three orders of magnitude lower, even at temperatures above 1050 °C and under highly reducing conditions.[9] The prevalent (high) ionic conductivity is achieved by the incorporation of yttria (Y_2O_3), as the substitution of Zr^{4+} with Y^{3+} is charge-compensated by the formation of oxygen vacancies, and thus, increases the oxygen-ion conductivity.[9,10] Using Kroeger−Vink notation, this substitution can be described by

$$Y_2O_3 \xrightarrow{ZrO_2} 2Y'_{Zr} + v_O^{\bullet\bullet} + 3O_O^{\times} \qquad (1)$$

where Y'_{Zr} denotes an Y^{3+} ion on the Zr^{4+} lattice sites with a single negative relative charge and $v_O^{\bullet\bullet}$ is the vacancy in the oxygen lattice with a double positive relative charge. $O_O^{\times}$ denotes a lattice oxygen ion with a relative charge of zero. In addition, adding more than about 7−8 mol % yttria stabilizes the cubic structure of zirconia, thereby further facilitating the movement of oxygen ions in the solid. A maximum in oxygen-ion conductivity is typically achieved with around 10 mol % of Y_2O_3.[11] At higher yttria content, defect interactions start to prevail, reducing the mobility of ions, and thus, the ionic conductivity of the solid solution.[12] Consequently, different approaches have been investigated in the past decades to alter the transport properties of oxide ceramics. Aside from doping/substitution, major efforts have been devoted to tailoring the ionic and electronic partial conductivities by micro- and/or nanostructuring.[13,14] The introduction of additional interfaces, such as grain boundaries or free surfaces, can significantly affect a material's defect chemistry due to the formation of a space-charge region at the interface.[10,15−18] It is well-known that grain boundaries of oxygen-ion conducting ceramics, such as YSZ and ceria, are characterized by a positively charged grain-boundary core, which results in depletion of oxygen vacancies at the grain boundary and accumulation of electrons.[10,16,17] Consequently, the grain boundaries act as a barrier to the transport of oxygen vacancies, eventually decreasing the overall

Received: April 22, 2025
Revised: June 7, 2025
Accepted: June 16, 2025
Published: June 26, 2025

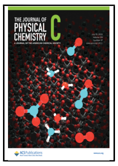

https://doi.org/10.1021/acs.jpcc.5c02744
J. Phys. Chem. C 2025, 129, 12585−12594

ionic conductivity. In polycrystalline oxide ceramics, the character of grain boundaries can be probed using electrochemical impedance spectroscopy (EIS), where an additional semicircle arises in the midfrequency range due to differences in dielectric relaxation time for transport through the grains and across the grain boundaries.[19−21] The impact of grain boundaries becomes more severe when the mean grain size is reduced to the nanoscale. Then, the space-charge region extends over the whole grain, and its properties determine the overall behavior of the material.[22] A prominent example is undoped or weakly doped nanocrystalline ceria, where the accumulation of electrons in the space-charge region of the grain boundaries results in prevailing electronic conductivity.[23,24] In contrast, bulk or microcrystalline ceria with a low grain boundary density exhibits dominant ionic conductivity with a negligible electronic conductivity contribution.

While extensive research efforts have been devoted to the impact of grain boundaries on the electrical properties of ceria- and zirconia-based ceramics,[16−18] studies on the effect of a high free surface area and the resulting surface space-charge region on defect chemistry, charge transport, and/or charge storage in the solid framework of porous materials are scarce. This is somewhat surprising, as nanoporous oxides with a high specific surface area are used in a number of electrochemical devices, for example as electrode materials in batteries as well as for gas sensing or photocatalytic applications.[25] A high surface area offers a large number of active sites for redox reactions to occur and has been shown to enable surface protonic conductivity.[26−29] Moreover, it can also result in additional pseudocapacitive charge-storage contribution due to the presence of a space-charge region at the interface,[30,31] making profound understanding of the impact of free surfaces on the electrochemical properties of porous oxides indispensable.

In this study, we present the electrochemical characterization of dense and porous, nanocrystalline 9.5 mol % yttria-stabilized zirconia thin films deposited by pulsed laser deposition (PLD). Structural characterization via X-ray diffraction (XRD) and Raman spectroscopy confirms the cubic phase of the YSZ thin films. The films exhibit a random pore structure with average grain- and pore-sizes of about 40 nm and 17 to 20 nm, respectively, as estimated from atomic force microscopy (AFM) data. A comparable grain size of about 40 nm is also found for the dense YSZ thin films. EIS measurements conducted on the dense films indicate a $p(O_2)$-independent electrical conductivity, as expected from defect chemical considerations for the predominantly ionically conducting material. In contrast, the porous films exhibit a $p(O_2)$-dependent conductivity under reducing conditions, i.e., the conductivity decreases with increasing oxygen partial pressure, following a characteristic slope of $-1/8$. Measurements with ion-blocking electrodes demonstrate that the unique $p(O_2)$-dependence of the total conductivity arises from an unexpectedly high electronic conductivity contribution, which is several orders of magnitude larger than reference values for single crystals of YSZ.[9] The increased electronic partial conductivity is attributed to the presence of a surface space-charge region. The high reducibility results in a positive surface charge, which leads to the accumulation of electrons. This electron enrichment, which surpasses the electron concentration in the bulk, leads to enhanced electronic conductivity along the surface space-charge region, governing the transport properties of the porous thin films under highly reducing conditions. By means of finite element method (FEM) simulations of a surface space-charge region, the unexpected slope of $-1/8$ is reproduced when strong defect−defect interactions between electrons and oxygen vacancies are incorporated into the model. The results emphasize the profound impact that surface effects have on the defect chemistry and electrochemical properties of porous materials.

METHODS

The porous YSZ thin films were deposited on (0001)-oriented single-crystalline sapphire substrates by PLD. Deposition was performed using a KrF excimer laser having an energy of 2.3 J/cm^2 and a frequency of 10 Hz.[26] A cubic 9.5 mol % YSZ pellet served as the target. The substrate temperature was set to 300 °C, and the oxygen background pressure was 10 Pa. The as-prepared films were annealed at 800 °C for 3 days after deposition, which resulted in porous YSZ samples of approximately 70 nm thickness, as determined by profilometry (DektakXTL, Bruker). The same parameters were chosen for the deposition of dense YSZ thin films. Only the oxygen background pressure was reduced to 0.5 Pa. After annealing, the thickness of the dense YSZ samples was determined to be about 140 nm.

For impedance measurements, interdigital electrodes were prepared on top of the films by photolithography (positive photoresist, ma-P 1215, micro resist technology GmbH). Subsequently, platinum was deposited onto the resist structure and partially removed by a lift-off process.[32] The obtained electrodes with a thickness of about 200 nm consisted of 21 fingers of 3 mm length, having a width of 47 μm and a distance of 33 μm between the fingers. A schematic of the platinum electrode is shown in Figure 1(a). For measuring the electronic partial conductivity of the porous YSZ, macroscopic gold electrodes of thickness 400 nm were deposited on the thin films by thermal evaporation [see Figure 1(b)]. The dense gold electrodes can be considered as nonideal ion-blocking electrodes, due to the difference in electrode geometry, which reduces the triple-phase boundary for oxygen exchange by at least a factor of 25.

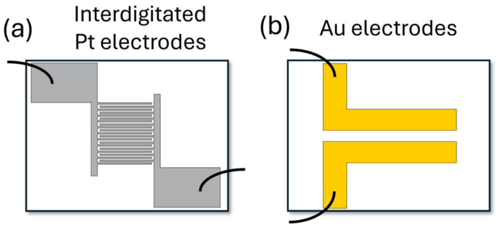

Figure 1. Schematics of the (a) interdigitated Pt electrodes and (b) macroscopic Au electrodes.

EIS was performed using a Novocontrol Alpha-A impedance bridge. Measurements were conducted on the sample with an AC amplitude of 100 mV and in the frequency range from 10 MHz to 10 mHz. The temperature was varied between 500 and 700 °C, and the oxygen partial pressure of the gas atmosphere was controlled by Ar/O_2 and CO/CO_2 mixtures. The gas mixture was dried over $CaCl_2$/P_2O_5 before flowing into the tube furnace. At each temperature and $p(O_2)$-measurement step, the sample was allowed to equilibrate for 4−6 h. Then, three measurements were performed to ensure

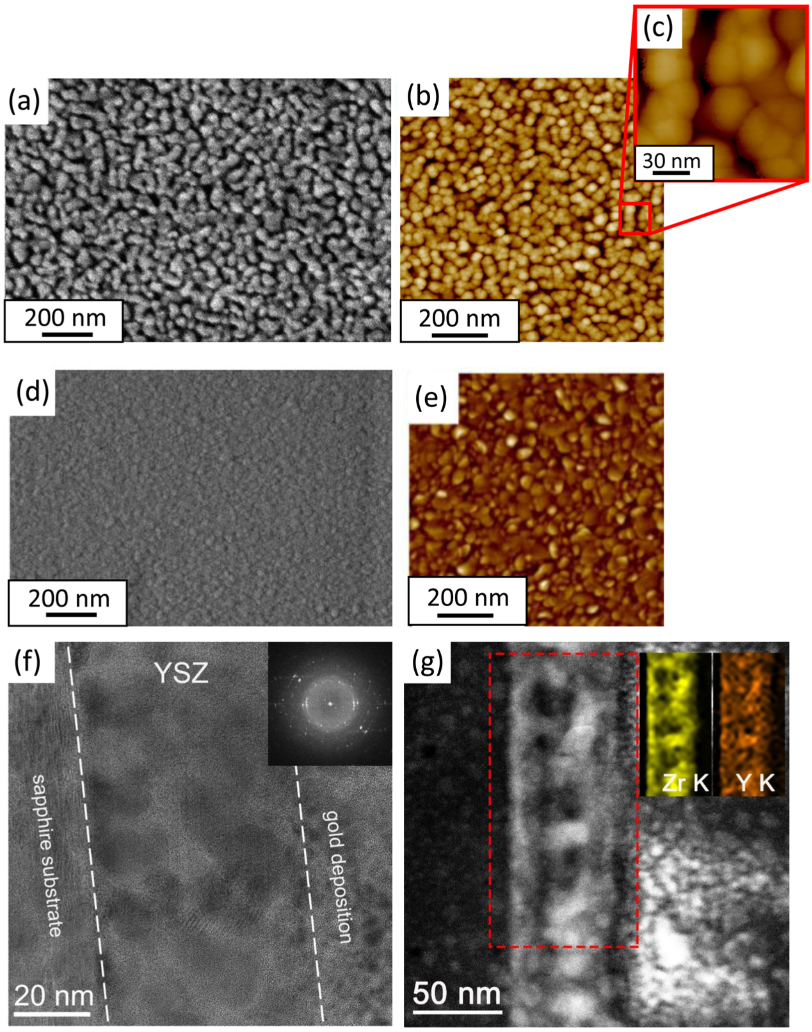

Figure 2. (a, d) Top-view SEM images and (b, c, e) AFM images of the porous and dense YSZ thin films after annealing at 800 °C. (f) High-resolution TEM image of the porous YSZ. (g) Scanning TEM elemental mapping of Zr and Y, revealing a uniform acceptor distribution across the porous YSZ.

reproducibility of the results. The obtained impedance spectra were analyzed using the software RelaxIS 3.

Structural and morphology characterizations were performed by scanning electron microscopy (SEM, MERLIN, Zeiss) at an acceleration voltage of 5 kV and by atomic force microscopy (AFM, MultiMode 8, Bruker) using a SiN cantilever in ScanAsyst mode. The AFM images were analyzed using NanoScope Analysis 1.9 and Gwyddion. Otsu's method was applied to calculate the porosity of the thin films.[33]

The crystallinity of the YSZ films was examined both by XRD using an X'Pert PRO MRD system from Malvern Panalytical Ltd. and by Raman spectroscopy using an InVia Raman microscope from Renishaw with an excitation wavelength of 633 nm.

Transmission electron microscopy (TEM) was performed using a Thermo Fisher Scientific Themis Z aberration-corrected microscope operated at 300 kV. The specimens for TEM analysis were prepared using an FEI STRATA 400 S dual-beam system with the Ga-ion beam operating at 30 kV, followed by final polishing at 2 kV for improving surface quality. A 5 nm thick gold coating was deposited onto the sample surface to improve conductivity and protect the porous YSZ during FIB lamella preparation, followed by ion beam deposition of a 1 μm thick carbon coating. The local elemental composition was determined by energy-dispersive X-ray spectroscopy (EDS) in scanning TEM (STEM) mode. The Zr K, Y K, and O K lines were used to map the spatial distribution of the respective elements.

RESULTS AND DISCUSSION

Structural Characterization. Figure 2(a) shows a representative top-view scanning electron microscopy (SEM) image of the porous 9.5 mol % YSZ thin films after annealing at 800 °C. Corresponding AFM images at different magnifications are presented in Figure 2(b),(c). Particularly in the AFM images, both the grains and grain boundaries are clearly distinguishable. Analysis yields an average grain size of (40 ± 2) nm, with pore sizes ranging from 15 to 20 nm. Using Otsu's method,[33] the average porosity was determined to be about 47%. SEM and AFM images of the dense thin films are presented in Figure 2(d),(e), revealing a comparable grain size and grain-boundary density. Additional information on the microstructure of the porous YSZ by means of transmission electron microscopy (TEM) investigations are provided in Figure 2(f),(g), confirming the structural results from the SEM and AFM characterizations. High-resolution TEM further

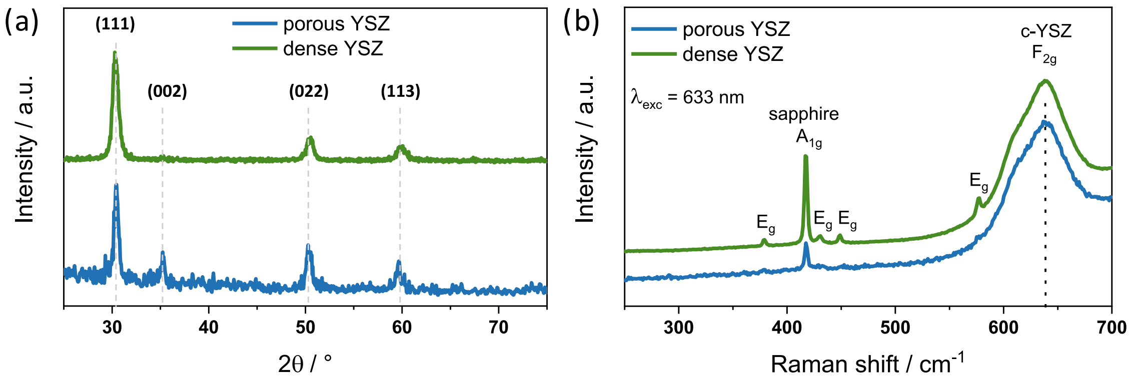

Figure 3. (a) XRD patterns and (b) Raman spectra of the porous and dense YSZ thin films after annealing at 800 °C.

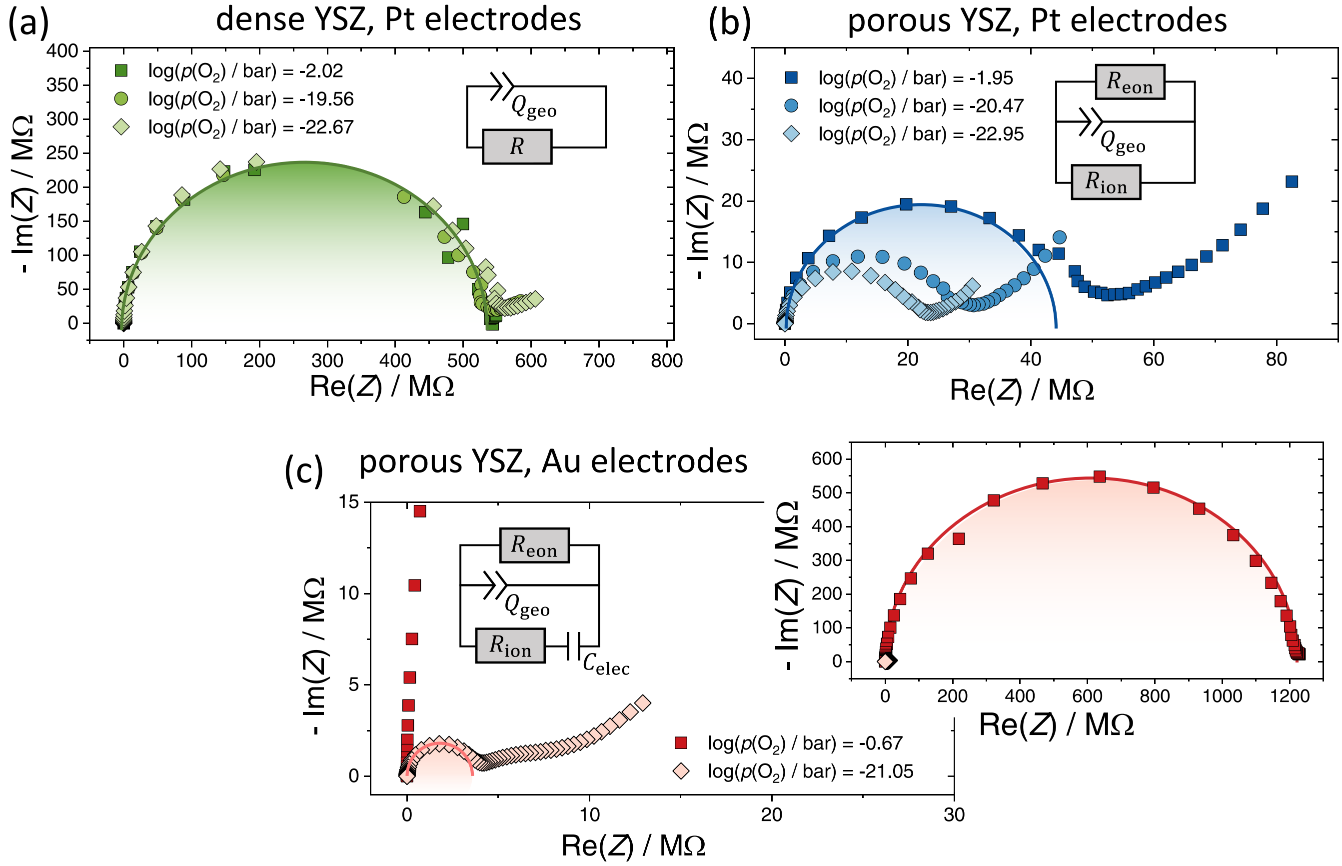

Figure 4. Comparison of the electrochemical impedance of (a) dense YSZ thin films measured using Pt electrodes and of porous YSZ thin films measured using (b) Pt electrodes and (c) Au electrodes at high and low oxygen partial pressures.

demonstrates the formation of cubic YSZ. No secondary phases were identified, neither in the grains nor at the grain boundaries. The elemental distribution determined by energy-dispersive X-ray spectroscopy (EDS) is presented in Figure 2(g). The dashed rectangle indicates the area probed, and the insets are the corresponding Zr and Y maps. No significant inhomogeneities were observed, meaning the Y acceptor is uniformly distributed throughout the porous YSZ thin films.

To confirm the cubic crystal structure, the dense and porous samples were also characterized by XRD and Raman spectroscopy (see Figure 3). Both films exhibit the characteristic reflections of cubic YSZ [see Figure 3(a)], indicating successful preparation of single-phase materials. Room-temperature Raman data reveal two dominant Raman modes [see Figure 3(b)]. The broad band around 640 cm^{-1} corresponds to the F_{2g} mode of YSZ, which is characteristic for the fluorite-type phase.[26] The asymmetric broadening of the F_{2g} mode is often observed for porous or nanocrystalline YSZ and probably arises from phonon confinement and/or strain due to the small grain size.[34,35] The band at 420 cm^{-1} can be assigned to the A_{1g} mode from the sapphire substrate used.[36,37] For the dense YSZ thin films, the same modes are apparent. No changes to the band positions were noticed, suggesting similar composition, as the F_{2g} mode is typically shifted to lower wavenumbers with increasing yttrium content.[38] The additional modes (E_{1g}) observed for the dense films are also arising from the sapphire substrate.[39]

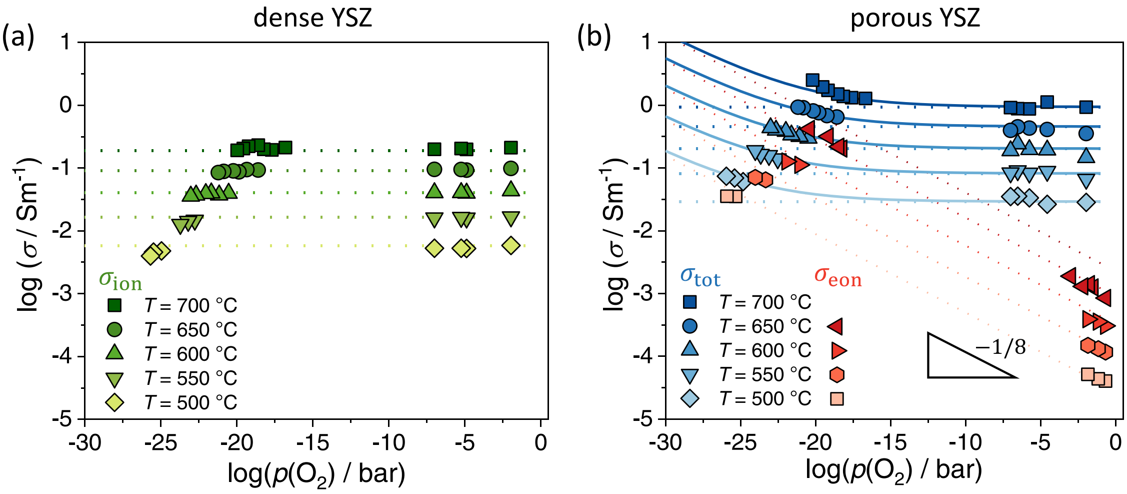

Figure 5. Oxygen partial pressure dependence of (a) ionic conductivity of the dense YSZ thin films and of (b) total and electronic conductivities of the porous YSZ thin films. Dotted and solid lines are fits to the experimental data.

Electrochemical Impedance Characterization. The conductivity of the dense and porous YSZ thin films was characterized in the temperature range between 500 and 700 °C, as well as for varying oxygen partial pressure [from $\log(p(O_2)/\mathrm{bar}) = -25$ to $\log(p(O_2)/\mathrm{bar}) = -0.6$], to investigate the impact of the free surface area on the electrical transport properties. Figure 4(a),(b) show the respective impedance spectra measured under highly reducing conditions. The dense samples [see Figure 4(a)] show the typical response of YSZ thin films.[32,40] One nearly ideal semicircle is observed in the high-to-mid frequency range, which corresponds to the transport through the dense material. Furthermore, the onset of an additional semicircle at low frequencies, representing the response of the electrode-electrolyte interface, is apparent from the data.[19,29] It is worth noting that no additional semicircle from the grain boundaries is visible, as the bulk and grain-boundary contributions overlap in nanocrystalline samples.[22,41,42] Therefore, the response corresponds to the total resistance of the nanocrystalline YSZ. In addition, the first semicircle is independent of oxygen partial pressure, which is consistent with dominant ionic conductivity, as expected for YSZ.[9]

The impedance spectra of the porous YSZ thin films are presented in Figure 4(b). The high-frequency semicircle reveals deviations from the ideal shape, in particular in the midfrequency range, indicating an overlapping transport process.[43,44] In addition, the size of the semicircle, and thus, the film resistance increases with decreasing oxygen partial pressure. Such a behavior suggests the presence of an electronic conductivity contribution, which is expected to decrease with increasing oxygen partial pressure, according to standard defect chemistry.[9] As shown in Figure 4(c), the impedance of the porous thin films exhibits an even more pronounced $p(O_2)$-dependence, and a significantly increased impedance at high oxygen partial pressure [$\log(p(O_2)/\mathrm{bar}) = -0.67$] when using Au electrodes, confirming the electrode's ion-blocking characteristics. Consequently, the impedance corresponds to the electronic contribution of the system.[43,45,46]

The total resistance of the dense YSZ thin films was determined by fitting an *RQ* element to the semicircle, where *R* corresponds to the resistance. The constant phase element (CPE) Q_{geo}, which represents the geometric capacitance of the sample, takes into account the minor nonideality of the semicircle [see Figure 4(a)]. For the porous YSZ thin films, an equivalent circuit for mixed ionic-electronic conductors was used,[43−45,47] consisting of two resistances R_{ion} and R_{eon} for the ions and electrons, respectively, and a CPE Q_{geo} [see Figure 4(b)]. From the CPE values, the geometric capacitance C_{geo} was calculated, yielding values of about 5×10^{-12} F for the dense samples and slightly higher values ranging from 6×10^{-12} to 7×10^{-11} F for the porous samples. These values are in reasonable agreement with those reported in the literature for mesoporous oxide thin films, which typically vary between 10^{-12} and 10^{-10} F.[26,43,48] An additional capacitance C_{elec} was included to account for the ion-blocking behavior of the Au electrodes [see Figure 4(c)]. The conductivity of both films was calculated from the resistance values assuming dense structures. Although this underestimates the conductivity of the porous samples,[41] it allows for direct comparison of the total and electronic conductivities, which were determined using Pt and Au electrodes with different cell constants.

Figure 5(a) presents the total conductivities of the dense YSZ thin films, which are independent of oxygen partial pressure. This confirms dominant oxygen-ion conductivity σ_{ion}, as expected for YSZ, the temperature-dependence of which is described by

$$\sigma_{\mathrm{ion}}(T) = \frac{\sigma^0_{\mathrm{ion}}}{T} \exp\left(-\frac{E_{\mathrm{A,ion}}}{k_B T}\right) \tag{2}$$

with σ^0_{ion} being the conductivity prefactor, k_B the Boltzmann constant, and $E_{\mathrm{A,ion}}$ representing the activation energy, which corresponds to the effective migration enthalpy of the oxygen ions ΔH_{mig}. The ionic conductivity of the dense YSZ thin films can be well described using eq 2, as indicated by the dotted lines in Figure 5(a), yielding $E_{\mathrm{A,ion}} = (1.2 \pm 0.05)$ eV. This is in excellent agreement with results from literature, where values of 1.10 eV to 1.24 eV have been reported for nanocrystalline YSZ.[26,49]

A $p(O_2)$-independent total conductivity, i.e., dominant ionic conductivity, was also observed for the porous YSZ thin films in the high oxygen partial pressure range, as shown in Figure 5(b). Applying eq 2 yields an activation energy of $E_{\mathrm{A,ion}} = (1.2 \pm 0.05)$ eV for ion transport, as in case of the dense YSZ samples. Interestingly, under highly reducing conditions, the σ_{tot} increased with decreasing oxygen partial pressure, indicating mixed ionic-electronic conductivity, according to the standard defect chemical description of binary oxides.[40,45,50]

The presence of a mixed ionic-electronic conductivity was also confirmed by the measurement of electronic conductivity using (ion-blocking) Au electrodes [see Figure 5(b)]. While the σ_{eon} in the high oxygen partial pressure range is about 4 orders of magnitude lower than σ_{ion}, it reaches comparable values to σ_{tot} under highly reducing conditions. This underscores the significant effect that the porosity has on the electronic properties of the YSZ thin films, as the electronic conductivity of single-crystalline YSZ is at least 3 orders of magnitude lower both under comparable atmospheric conditions and at even higher temperatures (∼1000 °C).[9] Hence, the electronic conductivity contribution in the porous YSZ thin films is increased by several orders of magnitude compared to σ_{eon} in the bulk material. In addition, the electronic conductivity of the porous thin films shows an unexpected $p(\mathrm{O_2})$-dependence with a characteristic slope of −1/8. In contrast, a slope of −1/4 is observed for single crystals of YSZ, as expected from defect chemical considerations.[9] The electronic conductivity contribution (dotted lines) can therefore be described by

$$\sigma_{\mathrm{eon}}(T) = \frac{\sigma'_{\mathrm{eon}}}{T}\exp\left(-\frac{E_{\mathrm{A,eon}}}{k_{\mathrm{B}}T}\right)p(\mathrm{O_2})^{-1/8} \tag{3}$$

yielding an activation energy of $E_{\mathrm{A,eon}} = (1.5 \pm 0.1)$ eV. As indicated by the solid lines in Figure 5(b), an excellent description of the measured total conductivity is achieved when considering both contributions, namely, $\sigma_{\mathrm{tot}} = \sigma_{\mathrm{ion}} + \sigma_{\mathrm{eon}}$. The unexpectedly high electronic partial conductivity, along with the unusual $p(\mathrm{O_2})$-dependence, evidently arises from the presence of a high surface area. Such effects may be attributed to surface space-charge regions formed around the grains of the porous thin films. Note that it can be ruled out that the electronic conductivity arises from space-charge effects involving the grain boundaries, since the dense thin films (having a similar grain-boundary density) only exhibit ionic conductivity over the entire oxygen partial pressure range investigated.

Finite Element Simulations. Finite element method (FEM) simulations were used to analyze the effect of a surface space-charge region on charge-carrier concentration and electronic partial conductivity of the porous YSZ thin films. For simplification, the nanoscale grains were described as a 1D system, where one edge represents the surface of a nanograin, while the other edge represents the center of the grain. A small region near the surface was defined, where the standard chemical potential of oxygen vacancy formation is lowered relative to the bulk by $\Delta\mu_{\mathrm{v}}^{\mathrm{o}} = \mu_{\mathrm{v,surf}}^{\mathrm{o}} - \mu_{\mathrm{v,bulk}}^{\mathrm{o}}$ to account for the positively charged surface.[51,52] The excess positive charge at the surface results in the formation of the space-charge layer, in which oxygen vacancies $\mathrm{v}_{\mathrm{O}}^{\bullet\bullet}$ are depleted and electrons e′ are accumulated. Since the samples were treated at 800 °C for 3 days, it can be assumed that the Y^{3+} ions on the Zr^{4+} lattice sites ($\mathrm{Y}'_{\mathrm{Zr}}$) are immobile. Consistent with the TEM analysis, we assumed that the acceptor-dopant concentration is uniform throughout the grains, i.e., a Mott−Schottky-type space-charge model is adopted. While this simplification may introduce quantitative deviations in the description of electrical properties,[53,54] it represents the most important characteristics of a space-charge layer under the given experimental conditions. In a first step, the electron concentration [e′] of the bulk was calculated using the expression given by Park and Blumenthal[9]

$$\begin{aligned}[\mathrm{e}'] &= \frac{2}{a^3}\cdot x(T, p(\mathrm{O_2})) \\ &= \frac{2}{a^3}\cdot 1.75\cdot\exp\left(-\frac{1.99\ \mathrm{eV}}{k_{\mathrm{B}}T}\right)\cdot\left(\frac{p(\mathrm{O_2})}{p^{\mathrm{o}}}\right)^{-1/4} \\ &= 2.83\times 10^{22}\frac{1}{\mathrm{cm}^3}\cdot\exp\left(-\frac{1.99\ \mathrm{eV}}{k_{\mathrm{B}}T}\right)\cdot\left(\frac{p(\mathrm{O_2})}{p^{\mathrm{o}}}\right)^{-1/4}\end{aligned} \tag{4}$$

with a being the lattice constant and $x(T,p(\mathrm{O_2})$ representing the nonstoichiometry. The prefactor 1.75 was determined by Park and Blumenthal from coulometric titration measurements conducted on single crystals of YSZ.

In the next step, the change in defect concentration in the space-charge region was calculated by solving the equilibrium conditions for the electrochemical potential of the electrons $\eta_{\mathrm{e}}(x)$ and the oxygen vacancies $\eta_{\mathrm{v}}(x)$[45]

$$\eta_{\mathrm{e}}(x) = \eta_{\mathrm{e}}^{\mathrm{bulk}} \quad \text{and} \quad \eta_{\mathrm{v}}(x) = \eta_{\mathrm{v}}^{\mathrm{bulk}} \tag{5}$$

where $\eta_{\mathrm{e}}^{\mathrm{bulk}}$ and $\eta_{\mathrm{v}}^{\mathrm{bulk}}$ denote the electrochemical potential of electrons and vacancies in the bulk, respectively. As the fraction of acceptor dopants $\mathrm{Y}'_{\mathrm{Zr}}$ exceeds 1% by far, it is reasonable to account for defect interactions, which are represented in the electrochemical potentials by terms that depend linearly on the defect concentrations. Therefore, neglecting gradient terms, the electrochemical potential $\eta_{\mathrm{v}}(x)$ of the oxygen vacancies can be described by[55]

$$\eta_{\mathrm{v}}(x) = \mu_{\mathrm{v}}^{\mathrm{o}} + k_{\mathrm{B}}T\ln\left(\frac{n_{\mathrm{v}}(x)}{1-n_{\mathrm{v}}(x)}\right) + \nu_{\mathrm{o,o}}f_{\mathrm{vv}}n_{\mathrm{v}} + \nu_{\mathrm{O,Zr}}f_{\mathrm{ev}}n_{\mathrm{e}} + 2e\phi(x) \tag{6}$$

where $\mu_{\mathrm{v}}^{\mathrm{o}}$ denotes the standard chemical potential of the vacancies, $\phi(x)$ is the electrical potential, and the second term represents the configurational contribution. n_{v} and n_{e} are the site fractions of oxygen vacancies and electrons, respectively, and f_{vv} and f_{ev} are the interaction parameters for the $\mathrm{v}_{\mathrm{O}}^{\bullet\bullet} - \mathrm{v}_{\mathrm{O}}^{\bullet\bullet}$ and the $\mathrm{v}_{\mathrm{O}}^{\bullet\bullet} - \mathrm{e}'$ interactions, respectively. $\nu_{\mathrm{o,o}} = 6$ and $\nu_{\mathrm{O,Zr}} = 4$ denote the coordination numbers of oxygen sites with the surrounding oxygen and zirconium sites, respectively. The electrochemical potential of electrons was defined in a similar way, where e′−e′ interactions are included by the interaction parameter f_{ee}. The electrical potential is linked to the defect concentration profiles by Poisson's equation

$$-\varepsilon_{\mathrm{r}}\varepsilon_0\frac{\mathrm{d}^2\phi}{\mathrm{d}x^2} = 2eN_{\mathrm{O}}n_{\mathrm{v}}(x) - eN_{\mathrm{Zr}}(n_{\mathrm{e}}(x) + n_{\mathrm{Y}}^{\mathrm{bulk}}) \tag{7}$$

with N_{O} and N_{Zr} being the density of oxygen and zirconium sites in the lattice, respectively, and $n_{\mathrm{Y}}^{\mathrm{bulk}} = 9.5\%$ representing the site fraction of yttrium ions.

The concentration profiles obtained from the solution to the Poisson equation were integrated over the entire space coordinate to calculate the overall integrated conductivity parallel to the surface, assuming a position-independent electron mobility u_{e}

$$\int_0^{l_{\mathrm{cell}}}\sigma_{\mathrm{e}}\,\mathrm{d}x = eN_{\mathrm{Zr}}u_{\mathrm{e}}\int_0^{l_{\mathrm{cell}}}n_e\,\mathrm{d}x \tag{8}$$

with l_{cell} = 20 nm being half of the average grain size. The conductivity was then obtained by dividing the integrated conductivity by the average grain size

$$\sigma_{\mathrm{e}} = \frac{1}{l_{\mathrm{cell}}} \int_0^{l_{\mathrm{cell}}} \sigma_{\mathrm{e}}\, \mathrm{d}x \tag{9}$$

The electron mobility was taken from the expression given by Park and Blumenthal[9]

$$u_{\mathrm{e}} = 8.02 \times 10^2 \frac{\mathrm{cm}^2}{\mathrm{Vs}} \exp\left(-\frac{1.89\ \mathrm{eV}}{k_{\mathrm{B}}T}\right) \tag{10}$$

FEM simulations were performed for varying oxygen partial pressures and for 700 and 1000 K to elucidate the effect of a surface space-charge region on electron concentration, and thus, the electronic conductivity of nanocrystalline YSZ. For the calculation of the defect concentration profile of the space-charge region, experimental values for the lattice constant (a = 5.1 Å) and permittivity (ε_{r} = 60) were taken from literature.[56−59] The difference in standard chemical potential of oxygen-vacancy formation between surface and bulk was set to be $\Delta\mu_{\mathrm{v}}^{\circ} = -1.5$ eV, which is a reasonable value for oxygen-ion conducting ceramics.[52,60,61] The $p(\mathrm{O_2})$-dependence of the carrier concentration profile was simulated for three different sets of interaction parameters, which are listed in Table 1.

Table 1. Interaction Parameters Used in the Simulations

parameter set	f_{vv}/eV	f_{ev}/eV	f_{ee}/eV
A	0	0	0
B	+0.2	−0.3	+0.2
C	+0.2	−0.4	+0.4

From eqs 9 and 10, the $p(\mathrm{O_2})$-dependence of electronic conductivity was calculated, which is depicted in Figure 6.

Figure 6(a) shows the $p(\mathrm{O_2})$-dependence of the electronic conductivity in a nanograin of YSZ without any defect interactions being taken into account (parameter set A). The data reproduce the characteristic slope of −1/4, which agrees with experimental results for dense samples and is well described by defect chemistry using Brouwer approximations for the intrinsic regime.[9] Interestingly, the characteristic slope decreases when interactions between oxygen vacancies and electrons are taken into account. For parameter set B [see Figure 6(b)], the slope changes to around −1/6, while the experimentally observed slope of −1/8 is reproduced for parameter set C [see Figure 6(c)]. From this data, it is evident that it is necessary to include defect−defect interactions in order to weaken the dependence of the defect concentration on oxygen partial pressure. We note that the set of parameters used to reproduce the experimental data is unlikely to be unique. However, the necessity to include defect−defect interactions for reproducing the experimental data hints toward a significantly increased electron concentration in the space-charge region at the free surface. In particular, the electron concentration exceeds the one present in the grain-boundary space-charge region, as no electronic conductivity contribution was found for the dense YSZ thin films (having a similar grain-boundary density). This may be attributed to a reduced space-charge potential at the grain boundaries, which has been found to be in the range of 0.15−0.25 eV.[62−64] The negative electron-vacancy interaction parameter $f_{\mathrm{ev}} = -0.4$ eV suggests trapping of electrons at the $\mathrm{Zr^{4+}}$ lattice sites next to oxygen vacancies, forming so-called T centers[65−67]

$$(\mathrm{v_O^{\bullet\bullet}Zr_{Zr}^{\times}})^{\bullet\bullet} + \mathrm{e'} \rightleftharpoons (\mathrm{v_O^{\bullet\bullet}Zr'_{Zr}})^{\bullet} \tag{11}$$

Furthermore, the positive electron−electron interaction parameter $f_{\mathrm{ee}} = +0.4$ eV may suggest that localization of two electrons next to one vacancy is unlikely. Hence, the high electronic conductivity in the surface space-charge region may simply arise from hopping of electrons between occupied and unoccupied $\mathrm{Zr^{4+}}$ ions localized next to oxygen vacancies. Theoretical calculations predict energies of about 1.9 eV for the transfer of electrons near oxygen vacancies.[68] This value is higher than the activation energy of $E_{\mathrm{A,eon}} = (1.5 \pm 0.1)$ eV determined from the analysis of the electronic conductivity contribution, indicating a reduced migration barrier for the hopping process in the surface space-charge region.

Finally, direct comparison with the experimental results reveals that our simulations underestimate the electronic partial conductivity by roughly 2 orders of magnitude. This deviation may indicate that the electrons within the space-

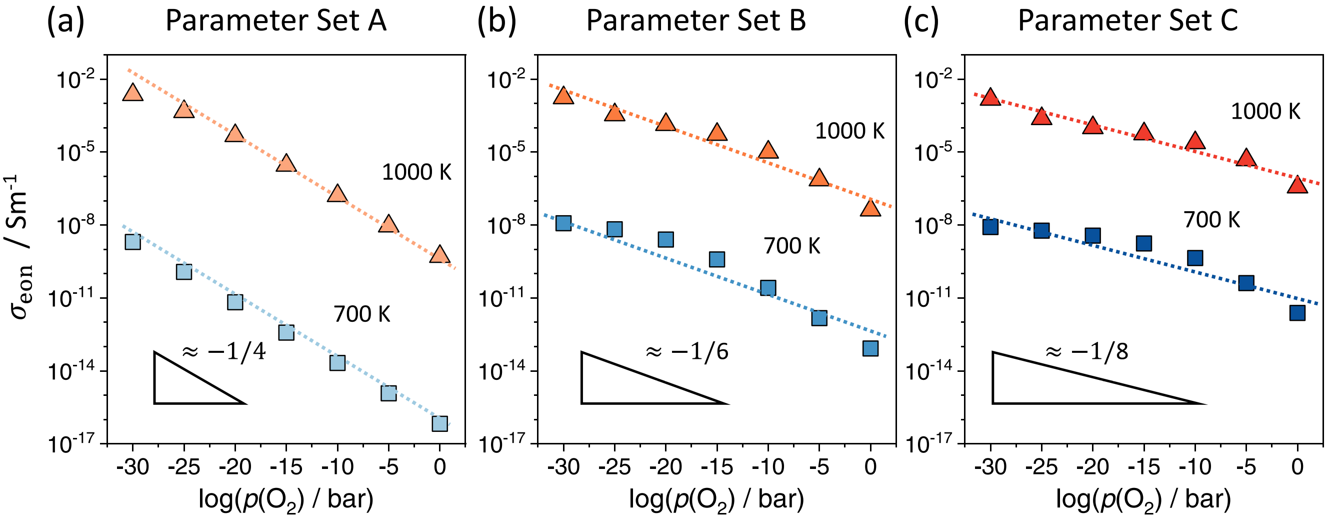

Figure 6. Calculated oxygen partial pressure dependences of the electronic conductivity at 700 and 1000 K for (a) parameter set A, (b) parameter set B, and (c) parameters set C of interaction parameters, namely, f_{vv}, f_{ev}, and f_{ee} (see Table 1). The dotted lines serve as guide for the eyes.

charge region possess a higher mobility than within the bulk, which is reasonable given the lower migration barrier for the hopping process [see eq 10]. However, more calculations are needed to clarify the transport mechanisms that are responsible for the high electronic conductivity of the porous YSZ thin films.

CONCLUSIONS

The impact of a high surface area on the electrochemical properties of yttria-stabilized zirconia (YSZ) was probed using electrochemical impedance spectroscopy. For this purpose, dense and porous thin films in nanocrystalline form were deposited by pulsed laser deposition. Structural characterization confirmed the successful preparation of cubic YSZ samples with similar grain sizes. Electrochemical characterization at various temperatures and over a broad oxygen partial pressure range indicated dominant ionic conductivity for the dense thin films, in line with expectations. In contrast, the porous thin films exhibited an unexpectedly high electronic conductivity contribution, dominating the total conductivity under highly reducing conditions. The increase in electronic conductivity by at least 3 orders of magnitude compared to that of single-crystalline YSZ is attributed to the presence of a space-charge region at the free surface of the nanograins. By means of continuum simulations using the finite element method, we demonstrate that the measured $p(O_2)$-dependence of the electronic conductivity can be reproduced by a space-charge model that includes strong defect−defect interactions between oxygen vacancies and electrons. The results emphasize the strong impact of surface effects on the ionic and electronic transport properties in nanostructured ceramics. The latter can be exploited in the design of advanced solid electrolytes and mixed-conducting materials for next-generation device applications.

AUTHOR INFORMATION

Corresponding Author

Matthias T. Elm − *Center for Materials Research (ZfM) and Institute of Experimental Physics I, Justus-Liebig University Giessen, 35392 Giessen, Germany;* orcid.org/0000-0001-7014-5772; Email: matthias.elm@exp1.physik.uni-giessen.de

Authors

Erdogan Celik − *Center for Materials Research (ZfM) and Institute of Experimental Physics I, Justus-Liebig University Giessen, 35392 Giessen, Germany*

Adrian Usler − *Institute of Physical Chemistry, RWTH Aachen University, 52074 Aachen, Germany;* orcid.org/0000-0001-5554-8485

Miguel Wiche − *Center for Materials Research (ZfM) and Institute of Applied Physics, Justus-Liebig University Giessen, 35392 Giessen, Germany*

Andrey Mazilkin − *Institute of Nanotechnology and Karlsruhe Nano Micro Facility (KNMFi), Karlsruhe Institute of Technology (KIT), 76131 Karlsruhe, Germany*

Torsten Brezesinski − *Institute of Nanotechnology, Karlsruhe Institute of Technology (KIT), 76131 Karlsruhe, Germany;* orcid.org/0000-0002-4336-263X

Roger A. De Souza − *Institute of Physical Chemistry, RWTH Aachen University, 52074 Aachen, Germany;* orcid.org/0000-0001-7721-4128

Complete contact information is available at: https://pubs.acs.org/10.1021/acs.jpcc.5c02744

Notes

The authors declare no competing financial interest.

ACKNOWLEDGMENTS

Financial support by the German Research Foundation (DFG) to T.B., grant no. BR 3499/5-1, and to M.T.E., grant nos. EL 863/3-1 and 512108624 (EL 863/8-1), is gratefully acknowledged. M.T.E. also acknowledges financial support by the Heisenberg program of the DFG (498993886, grant no. EL 863/6-1). The authors further acknowledge the support from the Karlsruhe Nano Micro Facility (KNMFi, www.knmf.kit.edu), a Helmholtz research infrastructure at Karlsruhe Institute of Technology (KIT, www.kit.edu).

REFERENCES

(1) Zakaria, Z.; Abu Hassan, S. H.; Shaari, N.; Yahaya, A. Z.; Boon Kar, Y. A Review on Recent Status and Challenges of Yttria Stabilized Zirconia Modification to Lowering the Temperature of Solid Oxide Fuel Cells Operation. *Int. J. Energy Res.* **2020**, *44* (2), 631−650.

(2) Minh, N. Q. Ceramic Fuel Cells. *J. Am. Ceram. Soc.* **1993**, *76* (3), 563−588.

(3) Holtappels, P.; Vogt, U.; Graule, T. Ceramic Materials for Advanced Solid Oxide Fuel Cells. *Adv. Eng. Mater.* **2005**, *7* (5), 292−302.

(4) Zhang, Y.; Zhang, P.; Ou, Z.; Cao, Z.; Feng, Q.; Mu, S.; Zhu, X.; Yang, W. YSZ-Based Dual-Phase Membrane Reactors for H2 Production by Coupling Water Splitting with CO_2 Capture. *Ind. Eng. Chem. Res.* **2024**, *63*, 16367−16375.

(5) Pirou, S.; Bermudez, J. M.; Hendriksen, P. V.; Kaiser, A.; Reina, T. R.; Millan, M.; Kiebach, R. Stability and Performance of Robust Dual-Phase $(ZrO_2)_{0.89}(Y_2O_3)_{0.01}(Sc_2O_3)_{0.10}$-$Al_{0.02}Zn_{0.98}O_{1.01}$ Oxygen Transport Membranes. *J. Membr. Sci.* **2017**, *543*, 18−27.

(6) Chen, C. S.; Kruidhof, H.; Bouwmeester, H. J. M.; Verweij, H.; Burggraaf, A. J. Oxygen Permeation through Oxygen Ion Oxide-Noble Metal Dual Phase Composites. *Solid State Ion* **1996**, *86−88* (PART 1), 569−572.

(7) Cirera, A.; Lpez-Gándara, C.; Ramos, F. M. YSZ-Based Oxygen Sensors and the Use of Nanomaterials: A Review from Classical Models to Current Trends. *J. Sens* **2009**, *2009* (1), No. 258489.

(8) Ramamoorthy, R.; Dutta, P. K.; Akbar, S. A. Oxygen Sensors: Materials, Methods, Designs and Applications. *J. Mater. Sci.* **2003**, *38* (21), 4271−4282.

(9) Park, J.; Blumenthal, R. N. Electronic Transport in 8 Mole Percent Y_2O_3 - ZrO_2. *J. Electrochem. Soc.* **1989**, *136* (10), 2867−2876.

(10) Guo, X.; Waser, R. Electrical Properties of the Grain Boundaries of Oxygen Ion Conductors: Acceptor-Doped Zirconia and Ceria. *Prog. Mater. Sci.* **2006**, *51* (2), 151−210.

(11) Filal, M.; Petot, C.; Mokchah, M.; Chateau, C.; Carpentier, J. L. Ionic Conductivity of Yttrium-Doped Zirconia and the "Composite Effect. *Solid State Ion* **1995**, *80* (1−2), 27−35.

(12) Clausen, K. N.; Hayes, W.; et al. Defect Structure of Yttria-Stabilized Zirconia and Its Influence on the Ionic Conductivity at Elevated Temperatures. *Phys. Rev. B* **1999**, *59* (22), 14202−14219.

(13) Maier, J. Pushing Nanoionics to the Limits: Charge Carrier Chemistry in Extremely Small Systems. *Chem. Mater.* **2014**, *26* (1), 348−360.

(14) Maier, J. Nanoionics: Ion Transport and Electrochemical Storage in Confined Systems. *Nat. Mater.* **2005**, *4* (11), 805−815.

(15) Maier, J. Ionic Conduction in Space Charge Regions. *Prog. Solid State Chem.* **1995**, *23* (3), 171−263.

(16) Guo, X. Physical Origin of the Intrinsic Grain-Boundary Resistivity of Stabilized-Zirconia: Role of the Space-Charge Layers. *Solid State Ion* **1995**, *81* (3−4), 235−242.

(17) Guo, X.; Waser, R. Space Charge Concept for Acceptor-Doped Zirconia and Ceria and Experimental Evidences. *Solid State Ion* **2004**, *173* (1−4), 63−67.

(18) Guo, X.; Maier, J. Grain Boundary Blocking Effect in Zirconia: A Schottky Barrier Analysis. *J. Electrochem. Soc.* **2001**, *148* (3), No. E121.

(19) Irvine, J. T. S.; Sinclair, D. C.; West, A. R. Electroceramics: Characterization by Impedance Spectroscopy. *Adv. Mater.* **1990**, *2* (3), 132−138.

(20) Eckhardt, J. K.; Burkhardt, S.; Zahnow, J.; Elm, M. T.; Janek, J.; Klar, P. J.; Heiliger, C. Understanding the Impact of Microstructure on Charge Transport in Polycrystalline Materials Through Impedance Modelling. *J. Electrochem. Soc.* **2021**, *168* (9), No. 090516.

(21) Fleig, J.; Maier, J. The Impedance of Ceramics with Highly Resistive Grain Boundaries: Validity and Limits of the Brick Layer Model. *J. Eur. Ceram Soc.* **1999**, *19* (6−7), 693−696.

(22) Kosacki, I.; Anderson, H. U. Microstructure - Property Relationships in Nanocrystalline Oxide Thin Films. *Ionics* **2000**, *6* (3−4), 294−311.

(23) Kim, S.; Maier, J. Partial Electronic and Ionic Conduction in Nanocrystalline Ceria: Role of Space Charge. *J. Eur. Ceram Soc.* **2004**, *24* (6), 1919−1923.

(24) Kim, S.; Maier, J. On the Conductivity Mechanism of Nanocrystalline Ceria. *J. Electrochem. Soc.* **2002**, *149* (10), J73.

(25) Celik, E.; Ma, Y.; Brezesinski, T.; Elm, M. T. Ordered Mesoporous Metal Oxides for Electrochemical Applications: Correlation between Structure, Electrical Properties and Device Performance. *Phys. Chem. Chem. Phys.* **2021**, *23* (18), 10706−10735.

(26) Celik, E.; Negi, R. S.; Bastianello, M.; Boll, D.; Mazilkin, A.; Brezesinski, T.; Elm, M. T. Tailoring the Protonic Conductivity of Porous Yttria-Stabilized Zirconia Thin Films by Surface Modification. *Phys. Chem. Chem. Phys.* **2020**, *22* (20), 11519−11528.

(27) Stub, S. Ø.; Vøllestad, E.; Norby, T. Mechanisms of Protonic Surface Transport in Porous Oxides: Example of YSZ. *J. Phys. Chem. C* **2017**, *121* (23), 12817−12825.

(28) Stub, S. Ø.; Vøllestad, E.; Norby, T. Protonic Surface Conduction Controlled by Space Charge of Intersecting Grain Boundaries in Porous Ceramics. *J. Mater. Chem. A* **2018**, *6* (18), 8265−8270.

(29) Elm, M. T.; Hofmann, J. D.; Suchomski, C.; Janek, J.; Brezesinski, T. Ionic Conductivity of Mesostructured Yttria-Stabilized Zirconia Thin Films with Cubic Pore Symmetry—On the Influence of Water on the Surface Oxygen Ion Transport. *ACS Appl. Mater. Interfaces* **2015**, *7* (22), 11792−11801.

(30) Yue, J.; Suchomski, C.; Voepel, P.; Ellinghaus, R.; Rohnke, M.; Leichtweiss, T.; Elm, M. T.; Smarsly, B. M. Mesoporous Niobium-Doped Titanium Dioxide Films from the Assembly of Crystalline Nanoparticles: Study on the Relationship between the Band Structure, Conductivity and Charge Storage Mechanism. *J. Mater. Chem. A* **2017**, *5* (5), 1978−1988.

(31) Li, C.; Gu, L.; Guo, X.; Samuelis, D.; Tang, K.; Maier, J. Charge Carrier Accumulation in Lithium Fluoride Thin Films Due to Li-Ion Absorption by Titania (100) Subsurface. *Nano Lett.* **2012**, *12* (3), 1241−1246.

(32) Neumeier, J. J.; Elm, M. T.; Luerßen, B.; Janek, J. Platinum Microelectrodes on Gadolinia Doped Ceria Single Crystals − Bulk Properties and Electrode Kinetics. *Phys. Chem. Chem. Phys.* **2018**, *20* (12), 8294−8301.

(33) Otsu, N. Threshold Selection Method from Gray-level Histograms. *IEEE Trans Syst. Man Cybern* **1979**, *SMC-9* (1), 62−66.

(34) Konetschny, A.; Weinhold, M.; Heiliger, C.; Elm, M. T.; Klar, P. J. Polarization-Dependence of the Raman Response of Free-Standing Strained $Ce_{0.8}Gd_{0.2}O_2$ Membranes. *Phys. Chem. Chem. Phys.* **2021**, *23* (11), 6903−6913.

(35) Celik, E.; Cop, P.; Negi, R. S.; Mazilkin, A.; Ma, Y.; Klement, P.; Schörmann, J.; Chatterjee, S.; Brezesinski, T.; Elm, M. T. Design of Ordered Mesoporous CeO_2−YSZ Nanocomposite Thin Films with Mixed Ionic/Electronic Conductivity via Surface Engineering. *ACS Nano* **2022**, *16* (2), 3182−3193.

(36) Kadleíková, M.; Breza, J.; Veselý, M. Raman Spectra of Synthetic Sapphire. *Microelectronics J.* **2001**, *32* (12), 955−958.

(37) Aminzadeh, A.; Sarikhani-fard, H. Raman Spectroscopic Study of Ni/Al_2O_3 Catalyst. *Spectrochim Acta A Mol. Biomol. Spectrosc.* **1999**, *55* (7−8), 1421−1425.

(38) Hemberger, Y.; Wichtner, N.; Berthold, C.; Nickel, K. G. Quantification of Yttria in Stabilized Zirconia by Raman Spectroscopy. *Int. J. Appl. Ceram. Technol.* **2016**, *13* (1), 116−124.

(39) Jia, W.; Yen, W. M. Raman Scattering from Sapphire Fibers. *J. Raman Spectrosc.* **1989**, *20* (12), 785−788.

(40) Zahnow, J.; Bastianello, M.; Janek, J.; Elm, M. T. Defect Chemistry of Individual Grains with and without Grain Boundaries of Al-Doped Ceria Determined Using Well-Defined Microelectrodes. *J. Phys. Chem. C* **2022**, *126* (5), 2737−2746.

(41) Eckhardt, J. K.; Heiliger, C.; Elm, M. T. Understanding the Impedance of Mesoporous Oxides: Reliable Determination of the Material-Specific Conductivity. *ACS Appl. Mater. Interfaces* **2023**, *15* (29), 35332−35341.

(42) Tuller, H. L. Ionic Conduction in Nanocrystalline Materials. *Solid State Ion* **2000**, *131* (1), 143−157.

(43) Zahnow, J.; Bernges, T.; Wagner, A.; Bohn, N.; Binder, J. R.; Zeier, W. G.; Elm, M. T.; Janek, J. Impedance Analysis of NCM Cathode Materials: Electronic and Ionic Partial Conductivities and the Influence of Microstructure. *ACS Appl. Energy Mater.* **2021**, *4* (2), 1335−1345.

(44) Burkhardt, S.; Friedrich, M. S.; Eckhardt, J. K.; Wagner, A. C.; Bohn, N.; Binder, J. R.; Chen, L.; Elm, M. T.; Janek, J.; Klar, P. J. Charge Transport in Single NCM Cathode Active Material Particles for Lithium-Ion Batteries Studied under Well-Defined Contact Conditions. *ACS Energy Lett.* **2019**, *4* (9), 2117−2123.

(45) Maier, J. Physical Chemistry of Ionic Materials *Phys. Chem. Ionic Mater.*, 2004, DOI: 10.1002/0470020229.

(46) Jamnik, J.; Maier, J. Treatment of the Impedance of Mixed Conductors Equivalent Circuit Model and Explicit Approximate Solutions. *J. Electrochem. Soc.* **1999**, *146* (11), 4183−4188.

(47) Huggins, R. A. Simple Method to Determine Electronic Conductivity and Ionic Components of the Conductors in Mixed a Review. *Ionics* **2002**, *8* (3−4), 300−313.

(48) Hartmann, P.; Brezesinski, T.; Sann, J.; Lotnyk, A.; Eufinger, J.-P.; Kienle, L.; Janek, J. Defect Chemistry of Oxide Nanomaterials with High Surface Area: Ordered Mesoporous Thin Films of the Oxygen Storage Catalyst CeO_2−ZrO_2. *ACS Nano* **2013**, *7* (4), 2999−3013.

(49) Jiang, J.; Hertz, J. L. On the Variability of Reported Ionic Conductivity in Nanoscale YSZ Thin Films. *J. Electroceram* **2014**, *32* (1), 37−46.

(50) Tilley, R. J. D. Defects in Solids. *Defects in Solids* **2008**, 1−529.

(51) Lee, H. B.; Prinz, F. B.; Cai, W. Atomistic Simulations of Surface Segregation of Defects in Solid Oxide Electrolytes. *Acta Mater.* **2010**, *58* (6), 2197−2206.

(52) Zurhelle, A. F.; Tong, X.; Klein, A.; Mebane, D. S.; De Souza, R. A. A Space-Charge Treatment of the Increased Concentration of Reactive Species at the Surface of a Ceria Solid Solution. *Angew. Chem.* **2017**, *129* (46), 14708−14712.

(53) Parras, J. P.; Cao, C.; Ma, Z.; Mücke, R.; Jin, L.; Dunin-Borkowski, R.; Guillon, O.; De Souza, R. A. The Grain-Boundary Resistance of CeO_2 Ceramics: A Combined Microscopy-Spectroscopy-Simulation Study of a Dilute Solution. *J. Am. Ceram. Soc.* **2020**, *103* (3), 1755−1764.

(54) Usler, A. L.; De Souza, R. A.; Electrochem Soc, J.; D Jovic, Hc. V.; Barsoum, M. W. A Critical Examination of the Mott−Schottky Model of Grain-Boundary Space-Charge Layers in Oxide-Ion Conductors. *J. Electrochem. Soc.* **2021**, *168* (5), No. 056504.

(55) Mebane, D. S.; De Souza, R. A. A Generalised Space-Charge Theory for Extended Defects in Oxygen-Ion Conducting Electrolytes: From Dilute to Concentrated Solid Solutions. *Energy Environ. Sci.* **2015**, *8* (10), 2935−2940.

(56) Lawless, W. N. Evidence for Tunneling States in the Oxygen Conductor ZrO_2:Y_2O_3. *Phys. Rev. B* **1980**, *22* (6), 3122−3123.

(57) M'Peko, J. C.; Francis, J. S. C.; Raj, R. Impedance Spectroscopy and Dielectric Properties of Flash Versus Conventionally Sintered Yttria-Doped Zirconia Electroceramics Viewed at the Microstructural Level. *J. Am. Ceram. Soc.* **2013**, *96* (12), 3760−3767.

(58) Steil, M. C.; Thevenot, F.; Kleitz, M. Densification of Yttria-Stabilized Zirconia: Impedance Spectroscopy Analysis. *J. Electrochem. Soc.* **1997**, *144* (1), 390−398.

(59) Thompson, D. P.; Dickins, A. M.; Thorp, J. S. The Dielectric Properties of Zirconia. *J. Mater. Sci.* **1992**, *27* (8), 2267−2271.

(60) Sayle, T. X. T.; Parker, S. C.; Catlow, C. R. A. The Role of Oxygen Vacancies on Ceria Surfaces in the Oxidation of Carbon Monoxide. *Surf. Sci.* **1994**, *316* (3), 329−336.

(61) Wardenga, H. F.; Schuldt, K. N. S.; Waldow, S.; De Souza, R. A.; Klein, A. Surface Potentials of Acceptor- and Donor-Doped CeO_2 Thin Films and Their Relation to Oxygen Surface Exchange. *Phys. Chem. Chem. Phys.* **2022**, *24* (2), 1072−1080.

(62) Guo, X.; Maier, J. Grain Boundary Blocking Effect in Zirconia: A Schottky Barrier Analysis. *J. Electrochem. Soc.* **2001**, *148* (3), No. E121.

(63) Wang, J.; Conrad, H. Contribution of the Space Charge to the Grain Boundary Energy in Yttria-Stabilized Zirconia. *J. Mater. Sci.* **2014**, *49* (17), 6074−6080.

(64) Verkerk, M. J.; Middelhuis, B. J.; Burggraaf, A. J. Effect of Grain Boundaries on the Conductivity of High-Purity ZrO_2-Y_2O_3 Ceramics. *Solid State Ion* **1982**, *6* (2), 159−170.

(65) Azzoni, C. B.; Paleari, A. Sevenfold-and Sixfold-Coordinated Zr Ions in Cubic Stabilized Zirconia: Crystal-Field Approach. *Phys. Rev.* **1991**, *44*, 6858.

(66) Costantini, J. M.; Beuneu, F. Point Defects Induced in Yttria-Stabilized Zirconia by Electron and Swift Heavy Ion Irradiations. *J. Phys.: Condens. Matter* **2011**, *23* (11), 115902.

(67) Costantini, J. M.; Beuneu, F.; Morrison-Smith, S.; Devanathan, R.; Weber, W. J. Paramagnetic Defects in Electron-Irradiated Yttria-Stabilized Zirconia: Effect of Yttria Content. *J. Appl. Phys.* **2011**, *110* (12), No. 123506.

(68) Ramo, D. M.; Shluger, A. L. Structure and Spectroscopic Properties of Oxygen Divacancy in Yttrium-Stabilized Zirconia. *J. Phys. Conf. Ser.* **2008**, *117* (1), No. 012022.